

Thermal Control of Spin Excitations in the Coupled Ising-Chain Material RbCoCl_3

M. Mena,^{1,2} N. Hänni,^{3,4} S. Ward,^{2,5} E. Hirtenlechner,^{2,6} R. Bewley,⁷ C. Hubig,^{8,9} U. Schollwöck,⁸ B. Normand,¹⁰ K. W. Krämer,³ D. F. McMorrow,¹ and Ch. Rüegg^{5,10,11,12}

¹*London Centre for Nanotechnology and Department of Physics and Astronomy, University College London, Gower Street, London WC1E 6BT, United Kingdom*

²*Laboratory for Neutron Scattering and Imaging,*

Paul Scherrer Institute, CH-5232 Villigen PSI, Switzerland

³*Department of Chemistry and Biochemistry, University of Bern, Freiestrasse 3, CH-3012 Bern, Switzerland*

⁴*Physikalisches Institut, University of Bern, Siedlerstrasse 5, CH-3012 Bern, Switzerland*

⁵*Department of Quantum Matter Physics, University of Geneva, CH-1211 Geneva 4, Switzerland*

⁶*Institut Laue Langevin, CS 20156, F-38042 Grenoble, France*

⁷*ISIS Facility, STFC Rutherford Appleton Laboratory, Harwell Campus, Didcot OX11 0QX, United Kingdom*

⁸*Arnold Sommerfeld Center for Theoretical Physics,*

Ludwig-Maximilians-University Munich, 80333 München, Germany

⁹*Max-Planck-Institut für Quantenoptik, 85748 Garching, Germany*

¹⁰*Paul Scherrer Institute, CH-5232 Villigen PSI, Switzerland*

¹¹*Institute for Quantum Electronics, ETH Zürich, CH-8093 Zürich, Switzerland*

¹²*Institute of Physics, Ecole Polytechnique Fédérale de Lausanne, CH-1015 Lausanne, Switzerland*

(Dated: July 1, 2020)

We have used neutron spectroscopy to investigate the spin dynamics of the quantum ($S = 1/2$) antiferromagnetic Ising chains in RbCoCl_3 . The structure and magnetic interactions in this material conspire to produce two magnetic phase transitions at low temperatures, presenting an ideal opportunity for thermal control of the chain environment. The high-resolution spectra we measure of two-domain-wall excitations therefore characterize precisely both the continuum response of isolated chains and the “Zeeman-ladder” bound states of chains in three different effective staggered fields in one and the same material. We apply an extended Matsubara formalism to obtain a quantitative description of the entire dataset, Monte Carlo simulations to interpret the magnetic order, and finite-temperature DMRG calculations to fit the spectral features of all three phases.

Quantum systems that display one-dimensional (1D) nature [1] and Ising exchange [2] exhibit a very rich variety of phenomena. These include a gapped excitation continuum [3–5], excited bound states with emergent E_8 symmetry [6], quantum criticality [7–9], and topological excitations [10]. Recent intense interest in coupled Ising-chain physics was sparked by the ferromagnetic (FM) material CoNb_2O_6 [6, 11–13], whose spectrum of magnetic excitations is divided between a kinetic bound state and a two-domain-wall continuum, which itself splits into confined (E_8) bound states. The antiferromagnetic (AF) $\text{ACo}_2\text{V}_2\text{O}_8$ ($A = \text{Ba}, \text{Sr}$) compounds [14–17] have spiralling Ising chains with significant Heisenberg interactions, not only separating the transverse and longitudinal bound-state excitations [18, 19] but also realizing both uniform and staggered, longitudinal and transverse applied fields [15] in which to measure different types of bound state and critical behavior [10, 20–22]. However, both the response of a truly decoupled Ising chain and distinguishing the temperature dependences of all these features remain as challenging problems.

A paradigm for Ising-chain physics is provided by the ACoX_3 hexagonal perovskites [space group $P6_3/\text{mmc}$, shown in Figs. 1(a) and 1(b)], which include CsCoCl_3 [3, 4, 23–25], CsCoBr_3 [4, 5, 23, 24], RbCoCl_3 [24, 26], and TlCoCl_3 [27]. Their in-chain interactions are AF and

their spectra provided early examples of the continuum arising from pairs of moving domain walls (also referred to as “kinks” and “solitons”). Their special feature is that the Ising chains form a triangular lattice [Fig. 1(b)], frustrating the AF interchain interactions. They typically show two magnetic ordering transitions, which in RbCoCl_3 occur at $T_{N1} = 28$ K and $T_{N2} = 12$ K [28]. Thus, in contrast to CoNb_2O_6 and $\text{ACo}_2\text{V}_2\text{O}_8$, different chains experience different environments at different temperatures. Treating the neighboring chains as an effective staggered field, when this is zero one expects the spectrum of the isolated chain, a continuum with sinusoidal boundaries [29], whereas for finite staggered fields the spectrum is a Zeeman ladder of bound states [30].

In this Letter, we study the magnetic excitations of RbCoCl_3 in unprecedented detail by combining state-of-the-art instrumentation for neutron spectroscopy with a systematic thermal control of the different effective-field contributions. This allows an unambiguous separation of isolated-chain and staggered-field physics. Rising temperature causes both a band-narrowing and a broadening of bound and continuum features, as well as strong changes to the interchain coupling effects. These we explain by combining an extended Matsubara description with finite-temperature, time-dependent density-matrix renormalization-group (DMRG) calculations.

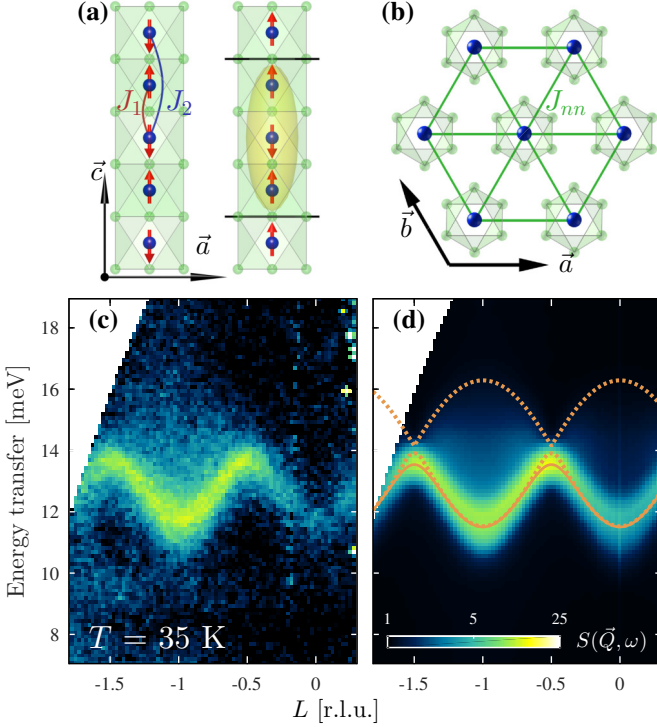


FIG. 1. (a) Schematic representation of chains in RbCoCl_3 . The Co^{2+} ions (blue) are embedded in Cl^- antiprisms (light green), an environment in which their ground state is an Ising doublet. The resulting effective $S = 1/2$ spins (red arrows) order antiferromagnetically along the c axis. The yellow ellipse denotes a pair of interacting domain walls. (b) Triangular lattice of chains in RbCoCl_3 . (c) Scattered intensity, $S(\vec{Q}, \omega)$, measured at 35 K. (d) $S(\vec{Q}, \omega)$ calculated by combining DMRG results with extended Matsubara analysis (see text). Dotted orange lines mark the edges of the continuum; the solid orange line marks the bound mode that separates from the continuum due to the interaction J_2 [panel (a)].

Three high-quality RbCoCl_3 single crystals of total mass 7.6 g were grown by the Bridgman technique in a moving vertical furnace [28] and coaligned in the (HHL) plane. Inelastic neutron scattering experiments were performed on the direct-geometry time-of-flight spectrometer LET (ISIS, UK) [31]. High-statistics data were collected with incident energy $E_i = 25$ meV and $(00L)$ perpendicular to the incident beam, at temperatures of 4, 18, and 35 K, i.e. in each magnetically ordered phase and above both. Lower-statistics data were collected at 8 K, 10.5 K, and 23 K with $E_i = 20$ meV. The data were corrected for detector efficiency and outgoing-to-incoming wave-vector ratio, k_f/k_i , using the program MANTID [32]. Data sets for the scattered intensity, $S(\vec{Q}, \omega)$, were analyzed with the HORACE software package [33].

We begin with an overview of the experimental data, which are shown in Fig. 1(c), Figs. 2(a,c,d), Figs. 3(a,c,d), and Figs. 4(a,b). First, we identify a band of excitations in the one-spin-flip (two-domain-wall) sector with a spin

gap of 11 meV and a cosinusoidal dispersion [Fig. 1(c)]. Second, our measurements confirm the strongly 1D nature of RbCoCl_3 , as shown in Sec. S1 of the Supplemental Material (SM) [34]. All data presented here were therefore averaged over H and K and binned as functions of the energy transfer and the momentum along L . In detail, the width of the band we observe at 35 K [Fig. 1(c)] far exceeds the instrumental resolution and its line shape [Fig. 4(a)] suggests a continuum. The spectrum sharpens at 18 K [Fig. 3(a)], presenting more lines with more intensity and less broadening [Figs. 3(c) and 3(d)]. At 4 K, the scattered intensity splits clearly into two different types of feature [Fig. 2(a)], a continuum [Fig. 2(c)] whose maximum disperses between 11 and 13.5 meV and a set of resolution-limited modes, the Zeeman ladder, whose lowest member [Fig. 2(d)] disperses between 12.5 and 14.5 meV. It is evident that thermal effects go beyond a simple line-broadening and include effective control of the staggered field due to the different 3D ordered phases.

To illustrate the influence of magnetic order on the measured Ising-chain dynamics, we have implemented a Cluster Heat Bath (CHB) Monte Carlo algorithm, as detailed in Sec. S2 of the SM [34]. Developed originally for studies of ACoX_3 compounds [38–40], CHB simulations below T_{N2} show well-ordered chains aligning to form domains of ferrimagnetic (FI) “honeycomb” planar order [40, 41], represented in the inset of Fig. 2(c). Interchain interactions are dominated by the nearest-neighbor (nn) AF coupling, J_{nn} [Fig. 1(b)], whose frustration leads to a massive degeneracy, and the FI order is selected by a weak FM next-nearest-neighbor (nnn) term, J_{nnn} [41]. The partially disordered AF (PDAF) [25, 41] state between T_{N2} and T_{N1} is characterized primarily by a decrease in FI interchain order [inset, Fig. 3(c)], while the staggered magnetization within each chain is also impacted weakly [28] by thermally excited domain walls [42]. Although 3D order is lost above T_{N1} , both susceptibility and diffuse scattering measurements [28] suggest that anomalously slow short-range correlations persist up to 60–80 K, and we will quantify this effect.

The Hamiltonian of a single Ising-Heisenberg chain with nn and nnn in-chain interactions [Fig. 1(a)] is

$$\mathcal{H} = \sum_j 2J_1[S_j^z S_{j+1}^z + \epsilon_1(S_j^x S_{j+1}^x + S_j^y S_{j+1}^y)] + h_j S_j^z + 2J_2[S_j^z S_{j+2}^z + \epsilon_2(S_j^x S_{j+2}^x + S_j^y S_{j+2}^y)], \quad (1)$$

where $|J_2| \ll J_1$, $\epsilon_1 \ll 1$, and h_j is the effective staggered field due to magnetic order. For this class of compounds, J_2 is thought to be FM [24]. An alternative approach [25] using only nn terms and including an anisotropic splitting of the Co^{2+} Kramers doublet is also thought [43] to provide a complete treatment of the orbital terms.

In this formalism, which we term the “Matsubara framework,” the matrix elements of Eq. (1) expressed

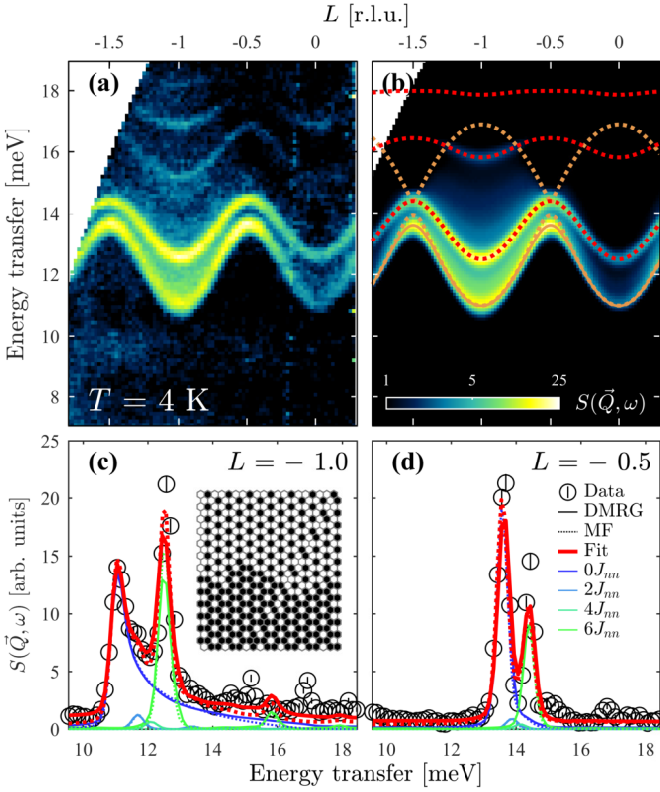


FIG. 2. (a) $S(\vec{Q}, \omega)$ measured at 4 K. (b) $S(\vec{Q}, \omega)$ calculated in Matsubara formalism (MF) with the parameters in the text. Orange lines as in Fig. 1(d). Red lines show the bound-state excitations of the Zeeman ladder. (c) and (d) $S(\vec{Q}, \omega)$ at 4 K (black symbols) integrated over windows $-1.05 < L < -0.95$ (c) and $-0.55 < L < -0.45$ (d). Red lines show optimized fits obtained by summing contributions from chains in different effective fields (blue-to-green lines). These panels are enlarged in Fig. S5 of the SM [34]. The inset in panel (c) shows a typical planar spin configuration, dominated by FI domains, obtained from CHB Monte Carlo simulations at $T < T_{N2}$; black hexagons denote up-spins and white down-spins.

in terms of the separation, ν , of two domain walls are

$$\begin{aligned}
 \langle 1 | \mathcal{H}(\vec{Q}) | 1 \rangle &= 2J_1(1 + \epsilon_1^2) + 2J_2[1 - \epsilon_2 \cos(2\pi L)] + h, \\
 \langle \nu | \mathcal{H}(\vec{Q}) | \nu \rangle &= 2J_1(1 + \frac{3}{2}\epsilon_1^2) + 4J_2 + \nu h, \\
 \langle \nu | \mathcal{H}(\vec{Q}) | \nu \pm 2 \rangle &= \epsilon_1 J_1 (1 + e^{\mp 2i\pi L}), \\
 \langle \nu | \mathcal{H}(\vec{Q}) | \nu \pm 4 \rangle &= -\frac{1}{2}\epsilon_1^2 J_1 (1 + e^{\mp 4i\pi L}), \quad (2)
 \end{aligned}$$

and $\langle \nu | \mathcal{H}(\vec{Q}) | \nu' \rangle = 0$ otherwise [24, 29, 43]. As noted above, the spectrum of this Hamiltonian forms a continuum when $h = 0$ [dashed orange lines in Figs. 1(d), 2(b), and 3(b)] and a Zeeman ladder when $h > 0$. With $h = 0$ but J_2 non-zero, an additional bound mode separates from the continuum around half-integer values of L [solid orange lines], while the intensity in the continuum shifts towards its lower edge. By calculating the spectral

weights from the Green function [29], the full dynamical structure factor shown in Fig. 2(b) was computed using Eq. (1) with the parameters discussed below.

Because J_{nnn} is much smaller than the instrumental resolution, at 4 K we model the effective staggered field by taking $h = mJ_{nn}$ with $m \in \{0, 2, 4, 6\}$. For perfect FI order, 2/3 of the sites experience a vanishing field, $h = 0$, and 1/3 a field $h = 6J_{nn}$; in practice, planar domain boundaries between different FI regions [inset Fig. 2(c)] produce small numbers of chains subject to the two intermediate fields. At 18 K, the PDAF regime presents a mix of all four staggered fields [inset Fig. 3(c)]. At 35 K, more detailed considerations are required as the chain environment becomes increasingly random.

Concerning in-chain dynamics at finite temperatures, the domain-wall pair excited by the scattered neutron is itself scattered by thermally excited domain walls [39, 42]. This increases the effective localization of both continuum and bound modes, as well as reducing their lifetimes, which changes the line shapes into Voigt functions with a constant Gaussian width of 0.32 meV (FWHM instrument resolution) and a temperature-dependent Lorentzian width, $\Gamma(T)$, which we take to be \vec{Q} -independent. In the Matsubara framework we model the band-flattening due to the increased localization by a temperature-driven decrease of ϵ_1 in Eq. (1) [44], taking ϵ_2 as a constant. Below we compute the spectral functions at all temperatures from DMRG calculations based only on the low- T parameters, and use the effective $\Gamma(T)$ and $\epsilon_1(T)$ as an aid to physical interpretation.

A fully quantitative account of continuum and bound-state energies, of line shapes, and of the overall scattered intensities [color contours in Figs. 2(b), 3(b), and 1(b)] is obtained with the parameter values $J_1 = 5.89(1)$ meV, $J_2 = -0.518(1)$ meV, $J_{nn} = 0.129(1)$ meV, and $\epsilon_2 = 0.605(1)$, valid at all temperatures, and with $\epsilon_1(T) = 0.126(1)$ at 4 K, 0.112(1) at 18 K, and 0.101(2) at 35 K [Fig. 4(c)]; $\Gamma(T) = 0.102(8)$ meV at 4 K and 0.25(1) meV at 18 K [Fig. 4(d)], and is not defined at 35 K (below). Figure 4(e) shows the optimized weights associated with chains in different effective fields at each temperature.

The separation of isolated-chain from staggered-field physics is clearest at 4 K [Fig. 2(a)]. The former is responsible for the 11 meV peak in Fig. 2(c), whose continuum tail extends to 17 meV, and the latter, with $h = 6J_{nn}$, for the sharp mode at 12.5 meV. The separation of these two primary contributions is emphasized by the small Γ and the near-absence of the intermediate staggered fields. We fit the relative weights of the staggered fields as 67(3), 3(3), 0(3), and 31(3)% for h from 0 to $6J_{nn}$, and thus the 0 and $6J_{nn}$ components are rather close to the ideal 2:1 ratio of the FI phase.

The most marked difference at 18 K [Fig. 3] is the strong shift towards contributions from the staggered fields $2J_{nn}$ and $4J_{nn}$, whose spectra overlap due both to their proximity in energy and to the increased Γ . The

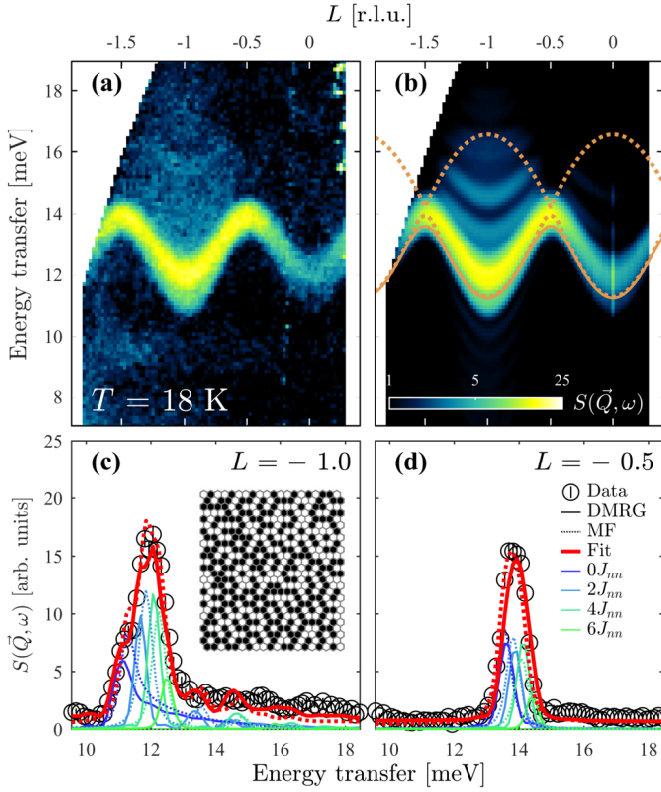


FIG. 3. (a) $S(\vec{Q}, \omega)$ measured at 18 K. (b) $S(\vec{Q}, \omega)$ calculated by DMRG. Orange lines as in Fig. 1(d). (c) and (d) Integrated scattered intensities following the conventions of Figs. 2(c) and 2(d). These panels are enlarged in Fig. S5 [34]. The inset in panel (c) shows a typical planar spin configuration in the PDAF phase from CHB Monte Carlo.

populations of the four staggered fields are 39(5), 35(5), 27(5), and 0(5)%, which lie close to our optimal CHB Monte Carlo results of 39, 35, 20, and 6%.

Finally, at 35 K one may expect interchain correlations to be lost and the scattering to be dominated by isolated-chain physics, as suggested by Fig. 1(c). However, in Fig. 4(a) it is clear that the isolated chain cannot provide an acceptable fit. To model the effects of thermal disorder, both in localizing the in-chain dynamics and in randomizing the chain environment, we have conducted Monte Carlo simulations of different static domain-wall distributions within the Matsubara framework, as described in Sec. S5 of the SM [34]. Qualitatively, we find a broadening dictated by $2J_{nn}$, that becomes independent of the chain-length distribution, and a shift of weight towards the band center that again is a localization effect reproduced using ϵ_1 . Quantitatively, however, a definitive fit of the 35 K data would require a systematic account of domain-wall dynamics.

For such a microscopic analysis of combined quantum and thermal fluctuations in the Ising chain, we have performed time-dependent DMRG calculations [45, 46] to obtain the finite-temperature spectral functions,

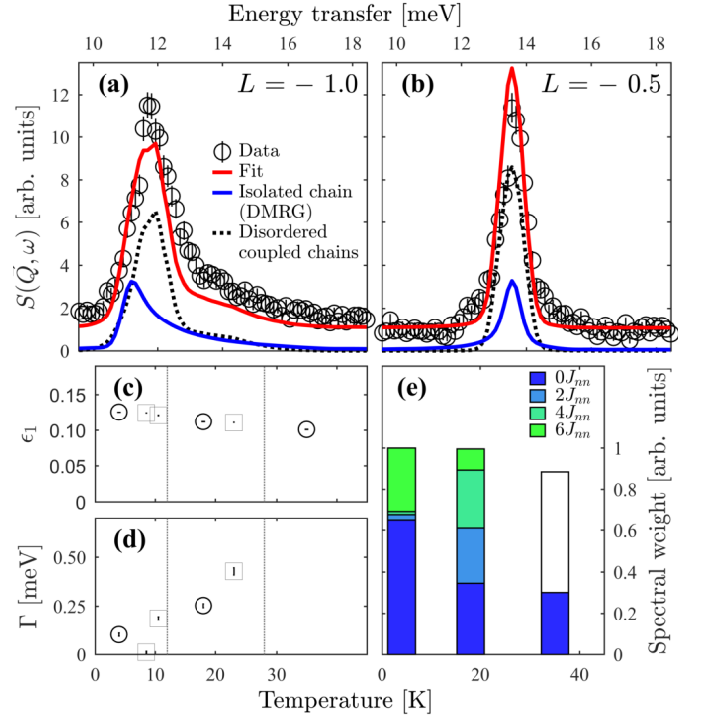


FIG. 4. (a) and (b) Integrated scattered intensities at 35 K following the conventions of Figs. 2(c) and 2(d). Red lines show fits combining DMRG for the isolated chain (solid blue) and Matsubara-framework modelling of coupled chains with static thermal disorder (dashed black lines). (c) Effective $\epsilon_1(T)$, with circles (squares) from fits to high- (low-) statistics datasets. (d) Effective Lorentzian width, $\Gamma(T)$. (e) Integrated intensity associated with each staggered field at 4 K and 18 K, taken from DMRG fits; at 35 K we distinguish the intensity (blue) associated with the isolated-chain response from that (white) due to chains in thermally disordered effective fields.

$S(\vec{Q}, \omega, T)$, as described in Sec. S3 of the SM [34]. The spatial and temporal evolution of a spin-flip excitation was computed for 512-site chains and a linear prediction method [47] used to access long effective times despite rapid entanglement growth at the higher temperatures. At 4 K we obtain the optimized DMRG parameters $J_1 = 5.86$ meV, $J_2 = -0.576$ meV, $J_{nn} = 0.128$ meV, $\epsilon_1 = 0.126$, and $\epsilon_2 = 0.559$. By including the different staggered fields and the instrumental resolution, we obtain the spectrum shown in Fig. 2(b), where the DMRG and extended Matsubara results are indistinguishable. For a quantitative visualization of the accuracy with which the experimental peaks and line shapes are reproduced, the DMRG results for all staggered fields are also shown as the solid blue-to-green lines in Figs. 2(c) and 2(d), and in detail in Sec. S4 [34].

DMRG captures all of the thermal broadening effects arising from domain-wall scattering in a single chain. As Fig. 3 makes clear, this provides an excellent account of the 18 K spectrum in all its details, although the fitted chain population distribution of 35, 27, 28, and 10% is

somewhat different from the less-constrained Matsubara fit (Sec. S4 [34]). At 35 K, where the approximation of chains in a well-ordered staggered field is no longer appropriate, we use our DMRG results for the scattered intensity, $I_0(\omega)$, of the isolated chain to reproduce the contributions of chains decoupled from their neighbors by thermal fluctuations. In combination with the contribution of chains coupled by the random fields of a thermal distribution of static domain walls, which as above we model in the Matsubara framework, our optimal fit to the measured intensity [Figs. 4(a) and 4(b)] reveals that approximately 63(5)% of the spectral weight, marked in white in Fig. 4(e), is contributed by chain segments in non-vanishing effective fields (Sec. S5 [34]). Thus we quantify the extent to which interchain correlations remain important at $T > T_{N1}$ [28], i.e. close to but above the regime of finite long-range order.

We comment that higher modes of the Zeeman ladder are observed in the spectrum between 15 and 18 meV. These are rather sharp at 4 K [Figs. 2(a) and 2(c)] but broad and weak at 18 K [Fig. 3(a)]. In our Matsubara and DMRG results [Fig. 2(b)], these modes are present with approximately the measured position, but their dispersion and intensity cannot be fitted with the same quantitative accuracy as the other spectral features. This suggests that higher-energy corrections [25] or an RPA-type extension of the Matsubara formalism may be required.

To summarize, we have studied both the continuum and the bound-state excitations of the quasi-1D AF Ising chain in a single material, RbCoCl_3 . By using temperature to control the type of 3D magnetic order, we measure the dynamical response in different effective magnetic fields. We model the continuum of the isolated chain, the Zeeman ladders in all staggered fields, and the broad response in thermally randomized fields by an analytical domain-wall formalism and by DMRG, to obtain a quantitative description of the spectrum in each of the temperature regimes investigated. Our results constitute a frontier in exploring the finite-temperature response of quantum spin systems and highlight the need for systematic theoretical methods to treat this problem in 3D.

We are grateful to R. Coldea and F. Essler for helpful discussions. We thank the neutron scattering facilities ISIS (Rutherford Appleton Laboratory, UK), SINQ (Paul Scherrer Institute, Switzerland), and the Institut Laue-Langevin (France). This research was supported by the UK Engineering and Physical Sciences Research Council (EPSRC) under Grant EP/N027671/1, by the European Research Council (ERC) under the EU Horizon 2020 research and innovation program Grants No. 681654 (HyperQC) and No. 742102 (QUENOCOBA), by the Bavarian Elite Network ExQM, and by the Swiss National Science Foundation (SNF) under Grants No. 200020-132877 and No. 200020-150257.

-
- [1] T. Giamarchi, *Quantum Physics in One Dimension*, (Oxford University Press, Oxford, 2004).
 - [2] E. Ising, Z. Phys. **31**, 253 (1925).
 - [3] H. Yoshizawa, K. Hirakawa, S. K. Satija, and G. Shirane, Phys. Rev. B **23**, 2298 (1981).
 - [4] S. E. Nagler, W. J. L. Buyers, R. L. Armstrong, and B. Briat, Phys. Rev. B **27**, 1784 (1983).
 - [5] S. E. Nagler, W. J. L. Buyers, R. L. Armstrong, and B. Briat, Phys. Rev. B **28**, 3873 (1983).
 - [6] R. Coldea, D. A. Tennant, E. M. Wheeler, E. Wawrzynska, D. Prabhakaran, M. Telling, K. Habicht, P. Smeibidl, and K. Kiefer, Science **327**, 177 (2010).
 - [7] S. Sachdev, Phys. World **12**, 33 (1999).
 - [8] H. M. Rønnow, R. Parthasarathy, J. Jensen, G. Aeppli, T. F. Rosenbaum, and D. F. McMorrow, Science **308**, 389 (2005).
 - [9] C. Kraemer, N. Nikseresht, J. O. Piatek, N. Tsyrlin, B. Dalla Piazza, K. Kiefer, B. Klemke, T. F. Rosenbaum, G. Aeppli, C. Gannarelli, K. Prokes, A. Podlesnyak, T. Strässle, L. Keller, O. Zaharko, K. W. Krämer, and H. M. Rønnow, Science **336**, 1416 (2012).
 - [10] Q. Faure, S. Takayoshi, S. Petit, V. Simonet, S. Raymond, L.-P. Regnault, M. Boehm, J. S. White, M. Månsson, Ch. Rüegg, P. Lejay, B. Canals, S. C. Furuya, T. Giamarchi, and B. Grenier, Nature Phys. **14**, 716 (2018).
 - [11] C. M. Morris, R. Valdés Aguilar, A. Ghosh, S. M. Koohpayeh, J. Krizan, R. J. Cava, O. Tchernyshyov, T. M. McQueen, and N. P. Armitage, Phys. Rev. Lett. **112**, 137403 (2014).
 - [12] N. J. Robinson, F. H. L. Essler, I. Cabrera, and R. Coldea, Phys. Rev. B **90**, 174406 (2014).
 - [13] I. Cabrera, J. D. Thompson, R. Coldea, D. Prabhakaran, R. I. Bewley, T. Guidi, J. A. Rodriguez-Rivera, and C. Stock, Phys. Rev. B **90**, 014418 (2014).
 - [14] S. Kimura, H. Yashiro, K. Okunishi, M. Hagiwara, Z. He, K. Kindo, T. Taniyama, and M. Itoh, Phys. Rev. Lett. **99**, 087602 (2007).
 - [15] S. Kimura, K. Okunishi, M. Hagiwara, K. Kindo, Z. He, T. Taniyama, M. Itoh, K. Koyama, and K. Watanabe, J. Phys. Soc. Japan **82**, 033706 (2013).
 - [16] A. K. Bera, B. Lake, W.-D. Stein, and S. Zander, Phys. Rev. B **89**, 094402 (2014).
 - [17] Z. Wang, M. Schmidt, A. K. Bera, A. T. M. N. Islam, B. Lake, A. Loidl, and J. Deisenhofer, Phys. Rev. B **91**, 140404 (2015).
 - [18] B. Grenier, S. Petit, V. Simonet, E. Canévet, L.-P. Regnault, S. Raymond, B. Canals, C. Berthier, and P. Lejay, Phys. Rev. Lett. **114**, 017201 (2015).
 - [19] A. K. Bera, B. Lake, F. H. L. Essler, L. Vanderstraeten, C. Hubig, U. Schollwöck, A. T. M. N. Islam, A. Schneidewind, and D. L. Quintero-Castro, Phys. Rev. B **96**, 054423 (2017).
 - [20] Z. Wang, J. Wu, S. Xu, W. Yang, C. Wu, A. K. Bera, A. T. M. N. Islam, B. Lake, D. Kamenskyi, P. Gogoi, H. Engelkamp, N. Wang, J. Deisenhofer, and A. Loidl, Phys. Rev. B **94**, 125130 (2016).
 - [21] M. Matsuda, H. Onishi, A. Okutani, J. Ma, H. Agrawal, T. Hong, D. M. Pajerowski, J. R. D. Copley, K. Okunishi, M. Mori, S. Kimura, and M. Hagiwara, Phys. Rev. B **96**, 024439 (2017).

- [22] Z. Wang, J. Wu, W. Yang, A. K. Bera, D. Kamenskyi, A. T. M. N. Islam, S. Xu, J. M. Law, B. Lake, C. Wu, and A. Loidl, *Nature* **554**, 219 (2018).
- [23] W. Lehmann, W. Breitling, and R. Weber, *J. Phys. C: Solid State Phys.*, **14**, 4655 (1981).
- [24] F. Matsubara, S. Inawashiro, and H. Ohhara, *J. Phys. Condens. Matter* **3**, 1815 (1991).
- [25] J. Goff, D. A. Tennant, and S. E. Nagler, *Phys. Rev. B* **52**, 15992 (1995).
- [26] D. J. Lockwood, I. W. Johnstone, H. J. Labbe, and B. Briat, *J. Phys. C: Solid State Phys.* **16**, 6451 (1983).
- [27] A. Oosawa, Y. Nishiwaki, T. Kato, and K. Kakurai, *J. Phys. Soc. Jpn.* **75**, 015002 (2006).
- [28] N. P. Hänni, D. Sheptyakov, U. Stuhr, L. Keller, M. Medarde, A. Cervellino, L.-P. Regnault, E. Hirtenlechner, M. Mena, Ch. Rüegg, and K. W. Krämer, unpublished.
- [29] N. Ishimura and H. Shiba, *Progr. Theor. Phys.* **63**, 743 (1980).
- [30] H. Shiba, *Progr. Theor. Phys.* **64**, 466 (1980).
- [31] R. I. Bewley, J. W. Taylor, and S. M. Bennington, *Nucl. Inst. Meth. Phys. Res. A* **637**, 128 (2011).
- [32] Available at <http://www.mantidproject.org> (online).
- [33] R. A. Ewings, A. Buts, M. D. Le, J. van Duijn, I. Bustinduy, and T. G. Perring, *Nucl. Inst. Meth. Phys. Res. A* **834**, 132 (2016).
- [34] For details see the Supplemental Material below, which contains Refs. [35–37].
- [35] F. Verstraete, J. J. Garcia-Ripoll, and J. I. Cirac, *Phys. Rev. Lett.* **93**, 207204 (2004).
- [36] J. Haegeman, C. Lubich, I. Oseledets, B. Vandereycken, and F. Verstraete, *Phys. Rev B* **94**, 165116 (2016).
- [37] T. Barthel, *New J. Phys.* **15**, 073010 (2013).
- [38] F. Matsubara, A. Sato, O. Koseki, and T. Shirakura, *Phys. Rev. Lett.* **78**, 3237 (1997).
- [39] O. Koseki and F. Matsubara, *J. Phys. Soc. Jpn.* **66**, 322 (1997).
- [40] O. Koseki and F. Matsubara, *J. Phys. Soc. Jpn.* **69**, 1202 (2000).
- [41] M. Mekata, *J. Phys. Soc. Jpn.* **49**, 76 (1977).
- [42] N. Todoroki and S. Miyashita, *J. Phys. Soc. Jpn.* **73**, 412 (2004).
- [43] H. Shiba, Y. Ueda, K. Okunishi, S. Kimura, and K. Kindo, *J. Phys. Soc. Jpn.* **72**, 2326 (2003).
- [44] A. J. A. James, W. D. Goetze, and F. H. L. Essler, *Phys. Rev. B* **79**, 214408 (2009).
- [45] U. Schollwöck, *Ann. Phys.* **326**, 92 (2011).
- [46] C. Hubig, I. P. McCulloch, and U. Schollwöck, *Phys. Rev B* **95**, 035129 (2017).
- [47] T. Barthel, U. Schollwöck, and S. R. White, *Phys. Rev. B* **79**, 245101 (2009).

Supplemental Material for "Thermal Control of Spin Excitations in the Coupled Ising-Chain Material RbCoCl_3 "

M. Mena, N. Hänni, S. Ward, E. Hirtenlechner, R. Bewley, C. Hubig, U. Schollwöck, B. Normand, K. W. Krämer, D. F. McMorrow, and Ch. Rüegg

S1. One-Dimensional Nature of RbCoCl_3

To justify the statement made in the main text that RbCoCl_3 is a very one-dimensional (1D) magnetic system, in Fig. S1 we show representative cuts of our scattered intensity data for \vec{Q} in the H direction with two choices of L . The broad lower and narrow upper excitations correspond respectively to the continuum and lowest bound-state features visible in Fig. 4 of the main text. The extremely flat dispersion in both normal directions is best modelled by a constant energy, i.e. any H - or K -dependence of the dispersion is smaller than the instrumental resolution.

S2. Cluster Heat Bath Monte Carlo Simulations

The Cluster Heat Bath (CHB) algorithm is a Monte-Carlo method that was developed specifically for simulating quasi-1D Ising compounds. In contrast to the Metropolis-Hastings algorithm, in which one spin is flipped at each time step, the CHB approach belongs

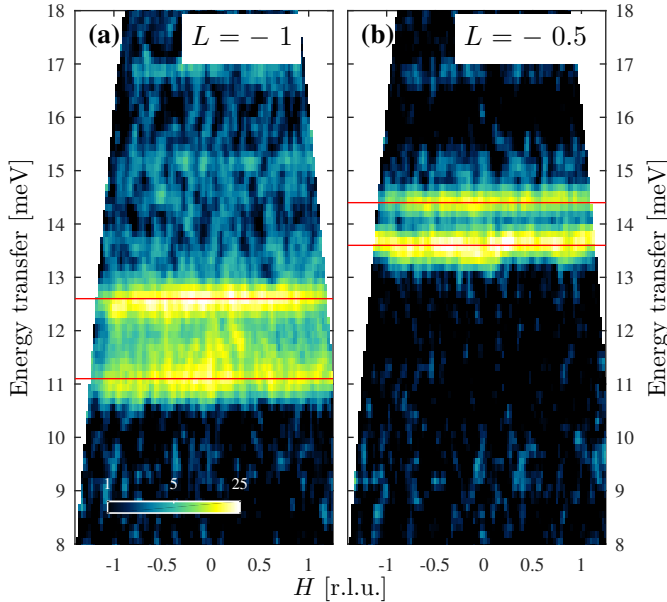


FIG. S1. Dynamical structure factors, $S(\vec{Q}, \omega)$, measured at 4 K for scattering vectors perpendicular to the chain direction. The intensity is integrated over the windows (a) $-1.05 < L < -0.95$ r.l.u. and (b) $-0.55 < L < -0.45$ r.l.u. The red lines are guides to the eye.

to the broad family of cluster methods, where blocks of many spins may be rearranged at each step. For the coupled Ising system, entire spin chains are flipped to achieve a configuration where every chain is in equilibrium (according to the Boltzmann distribution) with its environment at each step. This method has been used to reproduce closely the magnetic phase transitions of CsCoBr_3 and CsCoCl_3 and in the present study we have followed the work of Refs. [38–40].

Here we use CHB simulations in order to gain qualitative insight into and semi-quantitative comparisons with our experimental results. Specifically, we wish to illus-

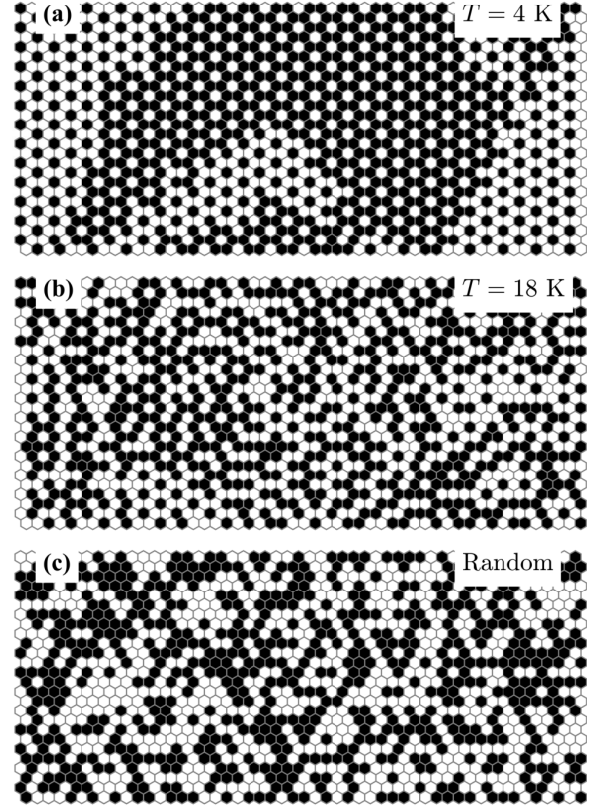


FIG. S2. Snapshots of spin configurations obtained from CHB simulations at temperatures corresponding to (a) 4 K and (b) 18 K in RbCoCl_3 . Each hexagon represents a site in a single plane of the triangular lattice of antiferromagnetically coupled Ising chains, which have in addition a weak ferromagnetic next-nearest-neighbor interaction. Black and white colors represent opposing directions of the staggered Ising order. (c) Fully random chain configuration.

trate the qualitative nature of the two ordered phases, shown in the insets of Figs. 2(c) and 3(c) of the main text, and to verify quantitatively the population factors, obtained by fitting the dynamical structure factor at each temperature, of chains subject to the different possible effective staggered fields. The CHB spin structure can also be used to simulate a quasi-elastic scattering signal for comparison with experimental observations [28], which show both sharp and broad temperature-dependent components. We have performed simulations, using the interaction parameters of the main text augmented by the value $J_{nnn} = -J_{nn}/10$, on lattices of $120 \times 120 \times 5000$ spins for up to 8000 steps. During even-numbered steps, 10 conventional CHB operations took place on randomly chosen chains (i.e. ten individual chains were flipped), while on odd-numbered steps flipping operations were allowed on loops of chains (of different, random lengths). The temperature of the system was lowered during the 8000 cycles, in a manner similar to simulated annealing, until the target temperature was obtained.

Figures S2(a) and S2(b) show examples of equilibrated spin configurations in a single plane obtained for temperatures corresponding respectively to 4 and 18 K in RbCoCl_3 . These are more extended versions of the figures shown in the insets of Figs. 2(c) and 3(c) of the main text. It is clear at 4 K [Fig. S2(a)] that significant domains of the system attain a well-ordered “honeycomb” pattern, in which 1/3 of the chains have a maximal net staggered field ($6J_{nn}$) while on 2/3 of them the field cancels. The contribution of other chain configurations is confined to the domain walls, which despite the rather weak J_{nn} in RbCoCl_3 are relatively sparse at 4 K. At intermediate temperatures [Fig. S2(b)], the domains are strongly disordered and the chains are correlated laterally only over rather short ranges, giving a distribution in which the staggered fields $2J_{nn}$ and $4J_{nn}$ have significant representation, whereas $6J_{nn}$ becomes much less likely. For reference we show in Fig. S2(c) a completely random planar spin configuration.

S3. Finite-temperature DMRG

For a microscopic understanding of temperature effects in the Ising spin chain, which in the extended Matsubara framework we described by effective parameters $\epsilon_1(T)$ and $\Gamma(T)$, we have performed time-dependent DMRG calculations at finite temperatures to obtain the full spectral functions. The spin system is represented in a basis of matrix-product states (MPS) [45, 46], in which the mixed states at finite temperatures are represented by a purification approach where their grand-canonical thermal density matrices are expressed in a doubled basis containing auxiliary variables [35, 47]. We computed the time evolution of a spin-flip excitation using the two-site time-dependent variational-principle method [36] in com-

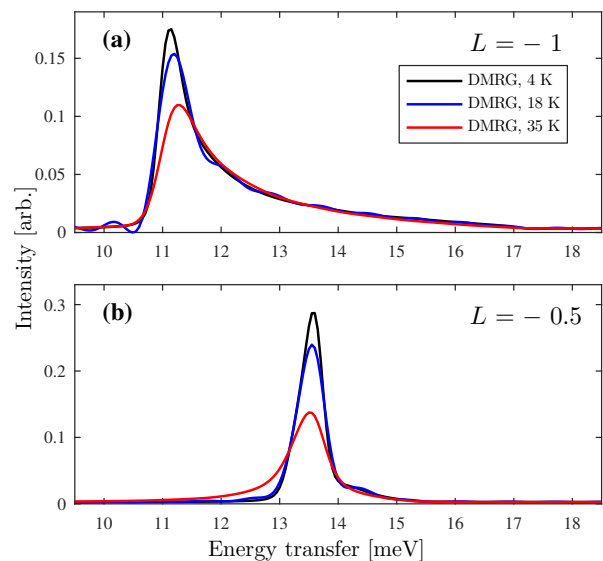


FIG. S3. $S(\vec{Q}, \omega)$ calculated by DMRG for the isolated Ising chain using the $T = 0$ interaction parameters of RbCoCl_3 with the instrumental broadening, $\sigma = 0.32$ meV, at temperatures of 4, 18, and 35 K for (a) $L = -1$ and (b) $L = -0.5$.

bination with the appropriate “near-optimal” auxiliary space transformation of Ref. [37].

Time evolution by repeated application of matrix operators causes a growth in information, and one of the primary attributes of the MPS formalism is to allow a systematic truncation of this information to fit the available computational resources. Physically, the problem of entanglement growth sets the limits in both time and space where a correlation function may be calculated with acceptable numerical precision. We have performed calculations for chain lengths up to $L = 512$ physical sites (1024 including auxiliary sites), finding these sufficient to exclude finite-size effects in the starting state in all cases. At $T = 4$ K, the growth of entanglement is not significant on the timescale over which excitations propagate across the finite system, and hence it is the system size that limits the maximum attainable time.

At $T = 18$ K and $T = 35$ K, the entanglement growth is more rapid, and this limits the maximum attainable time to $t_{\text{max}} \approx 70$ in units of $1/2J_1$ [Eq. (1) of the main text], where we set the criterion of numerical precision to be a maximal discarded weight of $\chi^2 = 10^{-8}$. However, one may then extend the computed data in time, for which the linear prediction method of Ref. [47] is particularly well suited when the finite temperature induces an exponential decay of the real-time correlators, as in the present problem. Optimizing the parameters of this interpolation scheme allowed us to stabilize the linear prediction for all momentum values and hence to reach large effective times, $t_{\text{max}}^{\text{pred}} \approx 2000$. We then evaluated the dynamical response function, $S(\vec{Q}, \omega, T)$, by two Fourier transformations of the DMRG correlation functions in

real space and time.

Figure S3 illustrates the results of our DMRG calculations for the case of an isolated chain (zero staggered field) at temperatures of 4, 18, and 35 K. The parameters J_1 , J_2 , and ϵ_2 are as given in the main text and Table S1, and we have included a broadening equivalent to the instrumental resolution of 0.32 meV. We stress that $\epsilon_1 = 0.126$ meV is fixed to its low-temperature value in all cases, i.e. it is not being changed as it is in our Matsubara procedure. Thus the fact that the peak in the continuum contribution at $L = -1$ moves up in energy with increasing temperature [Fig. S3(a)], signalling an effective band-narrowing, is an intrinsic consequence of the DMRG calculations capturing the effects of increased scattering processes involving thermally excited domain walls that are fully dynamical. We note that this intrinsic band-narrowing is smaller than the effective one providing optimal fits in the Matsubara framework, pointing to the need for a deeper investigation of dynamical domain-wall processes that lies beyond the scope of our present study. The $L = -0.5$ peak [Fig. S3(b)] is located near the band center and shows only a very weak downward trend with increasing temperature.

On the technical side, the weak oscillation in the 18 K data is a numerical artifact of the limited t_{\max} that is often suppressed by introducing a large effective broadening (analogous to the parameter Γ in the main text). Here we have investigated different broadening schemes, but guided by the physics we maintain the instrumental broadening, $\sigma = 0.32$ meV. In this way we do not obscure the intrinsic dynamical response, particularly the discrete Zeeman-ladder peaks in finite staggered fields shown in Figs. 2 and 3 of the main text and repeated in Sec. S4. As a consequence, the oscillation in the 18 K data in Fig. S3(a) is not eliminated completely, and its presence contributes percent-level errors in our DMRG intensity fits (Table S2) at this temperature; however, the line shape of the 35 K data takes its intrinsic form and this is important to our estimate of interchain correlations above T_{N1} (Sec. S5).

S4. Data and Fitting Comparisons: Ordered Phases

Here we show in full detail the comparison between our calculations within the extended Matsubara formalism and by DMRG, as well as the comparison of both with the spectral data measured at low ($T < T_{N2}$) and intermediate temperatures ($T_{N2} < T < T_{N1}$). The unique feature of the ACoX₃ materials is that, in both the fully ordered and the partially disordered antiferromagnetic phases, they allow the investigation of Ising chains subject to different effective staggered fields within a single material. This treatment assumes that the individual Ising chains remain as well-ordered clusters up to T_{N1} , leading to coherent effective staggered fields even as interchain

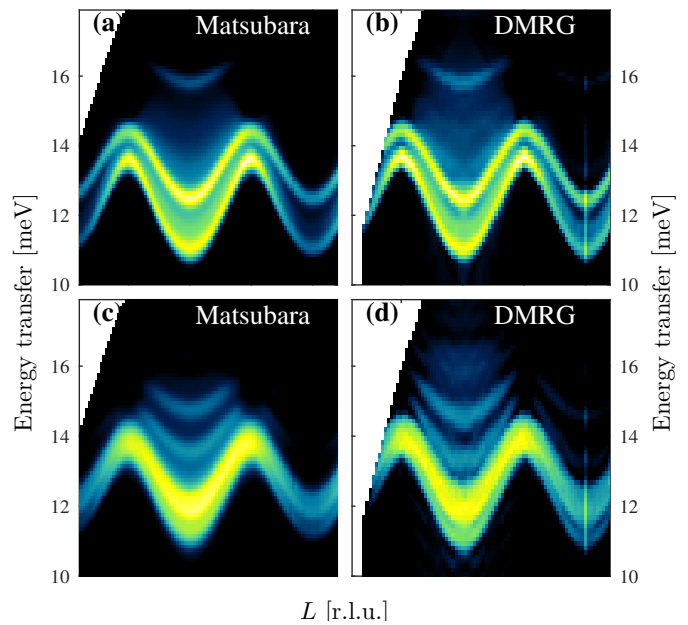


FIG. S4. Comparison between calculations of the dynamical structure factor, $S(\vec{Q}, \omega)$, performed within the extended Matsubara formalism (a,c) and by DMRG (b,d). Results are shown for the two temperatures at which detailed experimental data were gathered in the two ordered phases, namely 4 K (a,b) and 18 K (c,d).

correlations are weakened by the rising temperature. In Sec. S5 we will demonstrate that this assumption, which is also exploited in CHB simulations, is well justified at 18 K. By contrast, at $T > T_{N1}$ the loss of chain order due to thermal domain-wall formation becomes significant and an alternative treatment is required.

In Fig. S4 we show the full spectra obtained by extended Matsubara and by DMRG calculations. We note that Figs. S4(a) and S4(d) are the same, respectively, as Figs. 2(b) and 3(b) of the main text. While it is not surprising that both calculations reproduce the 4 K data rather well [Figs. S4(a) and S4(b)], this does demonstrate both that the Matsubara framework captures the primary physics of the system and that the DMRG methods are well within their numerical capabilities.

At 18 K, in the partially disordered antiferromagnetic phase, the level of agreement is non-trivial. In the extended Matsubara formalism, the fit to the data can, as discussed in the main text, be achieved by allowing only two of the six parameters to have a temperature-dependence, one affecting the band width and one the line width. By contrast, in DMRG there are no free parameters and both effects are intrinsic. Table S1 shows a comparison between the fitting results we obtain from the two procedures: there is close agreement on J_1 and J_{nn} , some discrepancy in the next-neighbor parameters J_2 and ϵ_2 , and of course the difference in treatment of the effective band width, contained in ϵ_1 .

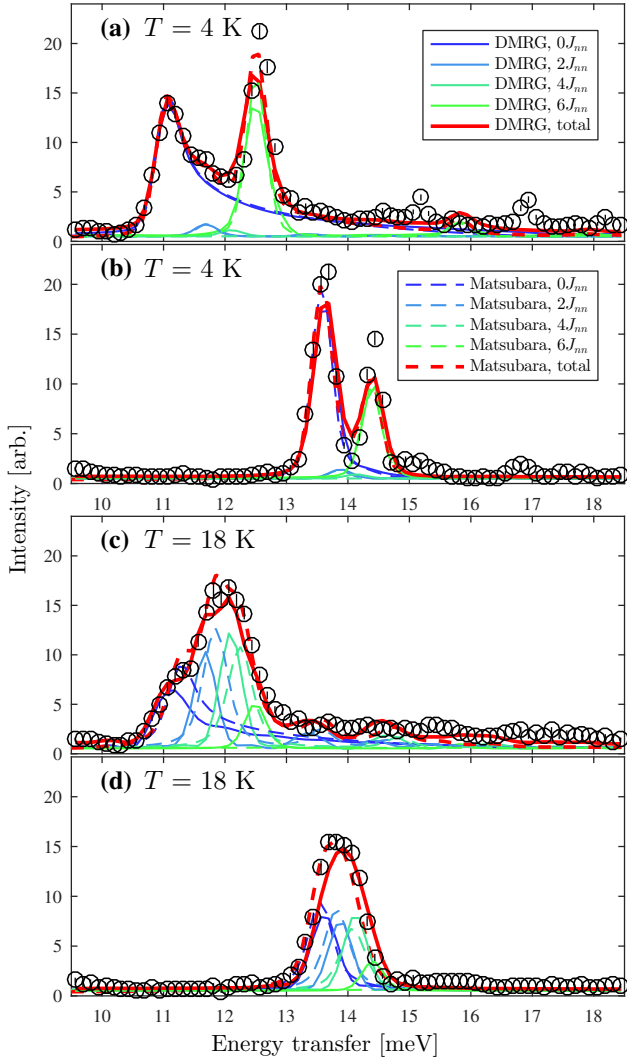


FIG. S5. Staggered-field contributions to the dynamical structure factor, $S(\vec{Q}, \omega)$. Measured intensities (points) and those calculated using both the extended Matsubara model (dashed lines) and DMRG (solid lines) are integrated over the \vec{Q} windows $-1.05 < L < -0.95$ r.l.u. (a,c) and $-0.55 < L < -0.45$ r.l.u. (b,d). Results are shown at temperatures of 4 K (a,b) and 18 K (c,d). The lines changing from blue to green indicate the individual contributions of chains subject to each of the possible staggered fields, mJ_{nn} with $m = 0, 2, 4$, or 6 , and the red lines show their sum.

These results are predicated on two subsidiary calculations, namely the intensity contributions due to chains in the different effective staggered fields and the weights of each chain type in the final sum; we take only the latter as free parameters. To show clearly the contributions of the different types of chain (i.e. different staggered fields) to the measured intensity, we have performed our calculations separately for staggered fields of $0, 2J_{nn}$, $4J_{nn}$, and $6J_{nn}$. The results, displayed in Figs. S5(a,b) and S5(c,d), show in full detail the respective panels of Figs. 2(c,d) and 3(c,d) of the main text. Both the energy levels of the

	Matsubara	DMRG
J_1 [meV]	5.89	5.86
J_2 [meV]	-0.518	-0.576
J_{nn} [meV]	0.129	0.128
ϵ_1 at 4 K	0.126	0.126
ϵ_1 at 18 K	0.112	0.126
ϵ_1 at 35 K	0.101	0.126
ϵ_2	0.605	0.559

TABLE S1. Comparison of fitting parameters obtained from the extended Matsubara Hamiltonian and from DMRG calculations at 4 K and 18 K. Error bars are omitted.

Method	T [K]	I_0	I_2	I_4	I_6
Matsubara	4	67(3)	3(3)	0(3)	31(3)
DMRG		65(3)	3(3)	1(3)	31(3)
CHB		61(1)	6(1)	5(1)	28(1)
Matsubara	18	39(5)	35(5)	27(5)	0(5)
DMRG		35(5)	27(5)	28(5)	10(5)
CHB		39(1)	35(1)	20(1)	6(1)

TABLE S2. Comparison of chain population factors deduced from extended Matsubara and DMRG calculations at 4 K and 18 K, and from CHB simulations on a system of 120×120 chains. I_m is the percentage of the scattered weight that may be ascribed to a chain in a staggered field $h = mJ_{nn}$. The sum of the intensities may deviate from 100% due to rounding effects. Because the measured $S(\vec{Q}, \omega)$ datasets contain many thousands of points, statistical errors in the fitting procedure are of order 0.1%. The quoted error bars for Matsubara and DMRG results represent the estimated systematic uncertainties in the fitting process, and for CHB in the simulations.

Zeeman ladders and the corresponding intensities computed within the extended Matsubara description and by DMRG are equal with quantitative accuracy at 4 K. However, it is clear at 18 K that the DMRG results do not contain as much narrowing of the band width as that optimizing the Matsubara fits, as a result of which the Zeeman-ladder states are less strongly renormalized and the weight factors appropriate to reproduce the measured intensity, shown in Table S2, include stronger contributions from higher m . Nonetheless, these discrepancies lie close to the systematic error bars on the fitted I_m percentages, and both fits are consistent with our CHB simulations (Sec. S2). One may certainly conclude that the treatment of neighboring chains in terms of an effective staggered field does provide an accurate reflection of the response of the 3D system in its ordered phases.

S5. Data and modelling above T_{N1}

For the discussion in Sec. S4 we excluded the high-temperature regime. In the magnetically disordered state, it is not appropriate to use a formalism based on effective staggered magnetic fields, i.e. on long segments of uniform interchain order. Nor, however, is it appro-

appropriate to neglect all interchain interactions at temperatures close to but above T_{N1} (Fig. 4(a) of the main text). In this regime, thermally induced randomness appears both in the chains, in the form of single thermal domain walls, and between the chains, in a form that can be modelled by an increasingly random effective field. In the Matsubara framework, a single domain wall acts to terminate each chain segment and we model the first effect by considering a static thermal distribution of domain walls, and hence of chain segment lengths, within a Monte Carlo approach. By applying the same approach to the neighboring chains, we also account for the second effect. Here it is important to note that our DMRG calculations, which are performed for a single chain at finite temperatures, are computing the first of these two effects for fully dynamic thermal domain walls.

In Figs. S6(a) and S6(b) we illustrate the results of the Matsubara-based procedure for the parameters of RbCoCl₃ with a very low broadening ($\sigma = 0.03$ meV). For long average segment lengths, $\langle n \rangle$, at $L = -1$ [Fig. S6(a)] the isolated-chain continuum and the Zeeman-ladder peaks for all three finite values of m are clearly discernible, along with faint signals for $-m$. At $L = -0.5$ [Fig. S6(b)], where the modes are non-dispersive, the intensities of the lowest modes of each Zeeman ladder, which have separation $2J_{nn}$, approach a 1:6:15:20:15:6:1 distribution, while the higher modes of all ladders are very weak. This regime is the basis on which, by inspection of the data at 18 K (Fig. 3 of the main text), one may conclude that the approach of effective staggered fields remains well justified at that temperature. As the density of thermal domain walls increases, i.e. as $\langle n \rangle$ decreases, it is clear at $L = -1$ that the low- T features lose weight and that scattered-intensity contributions appear at many different energies as chain segments of all possible lengths contribute (including those of only one and two spins). However, at $L = -0.5$ all of these segments continue to contribute at the same energies.

To model our 35 K data, we first restore the instrumental resolution, $\sigma = 0.32$ meV. As Figs. S6(c) and S6(d) make clear, this causes all of the separate features of the response at any average segment length to merge into a single, broad peak. Somewhat surprisingly, the shape of this feature, which at $L = -1$ is centered between the energies of the $m = 0$ and $m = 2$ peaks, becomes independent of $\langle n \rangle$. Thus although we cannot relate $\langle n \rangle$ directly to the temperature of the system, its effects become irrelevant due to the combined effects of the “splitting” $2J_{nn}$ and the instrumental broadening, which establish the width of the broad feature. Its position is controlled by the effective band-width parameter, ϵ_1 , which may therefore be fixed with reasonable accuracy using the experimental data. Beyond the fact that the domain walls in our modelling procedure are static rather than dynamic, which is also accounted for crudely by the

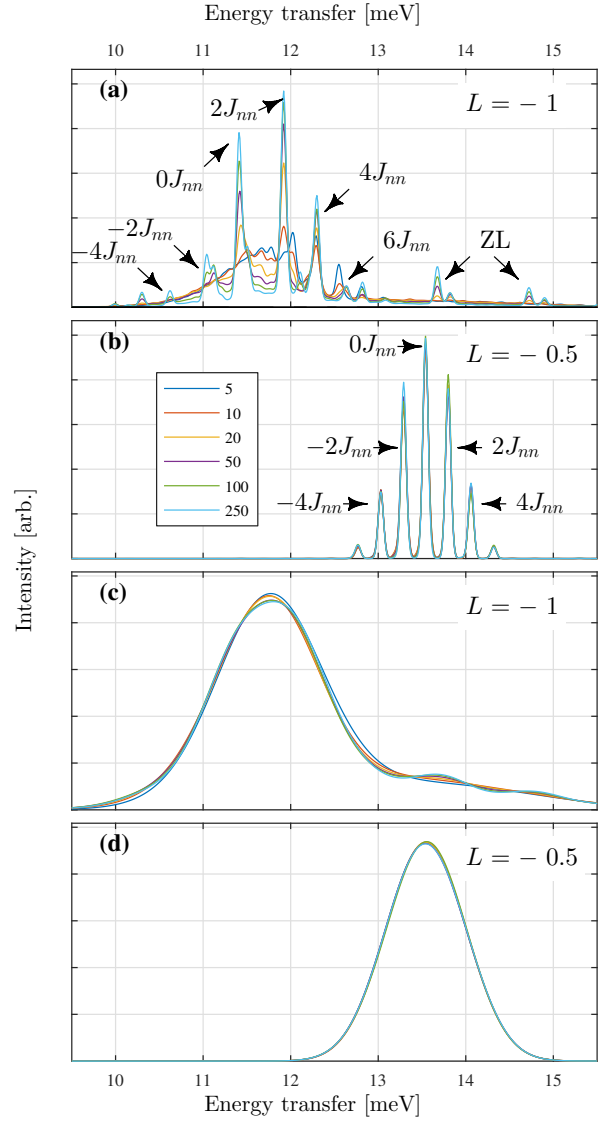


FIG. S6. Illustration of scattered intensities obtained by Monte Carlo modelling within the Matsubara framework for coupled chains in a thermally random effective field with the average length, $\langle n \rangle$, of the Ising chain segments as the adjustable parameter. All parameters are those of the Matsubara fit with effective band-width parameter $\epsilon_1 = 0.101$. (a) $L = -1$, $\sigma = 0.03$. (b) $L = -0.5$, $\sigma = 0.03$. (c) $L = -1$, $\sigma = 0.32$. (d) $L = -0.5$, $\sigma = 0.32$. The lowest modes of each Zeeman ladder are marked in panels (a) and (b) by “ mJ_{nn} ” and ZL denotes higher Zeeman-ladder modes in panel (a).

effective ϵ_1 , we expect the primary inaccuracy to lie in the neglected effects of J_2 across a thermal domain wall. In this sense the physics of coupled Ising-chain systems with thermal randomness poses a quantitative challenge to more specialized theoretical and numerical techniques.

Returning again to our experiments, it was shown clearly in the main text that, despite T exceeding T_{N1} , the scattered intensity at 35 K is far from that of chains isolated from each other by strong thermal fluctuations.

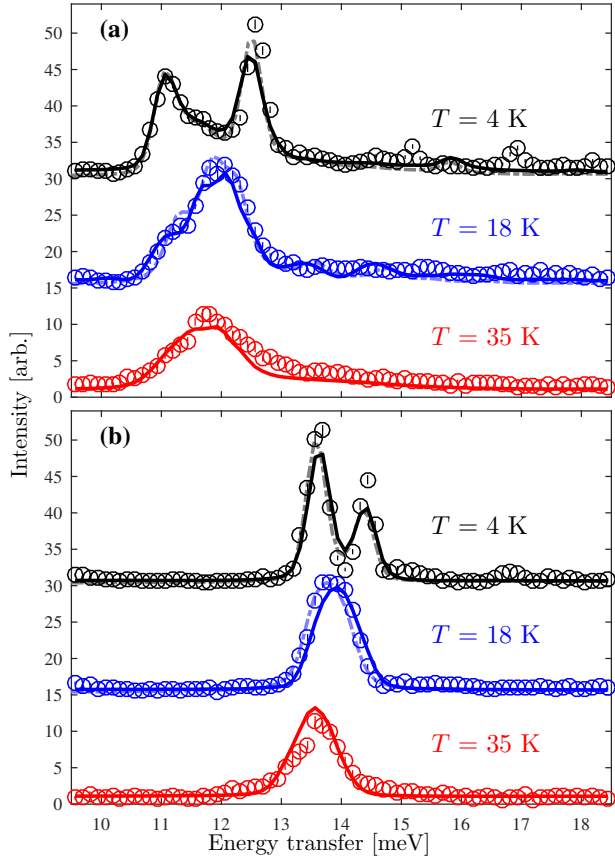


FIG. S7. Thermal evolution of $S(\vec{Q}, \omega, T)$, shown by superposing datasets taken at all three temperatures. Measured intensities (points) and those calculated using both the extended Matsubara model (dashed lines) and DMRG (solid lines) are integrated over the \vec{Q} windows (a) $-1.05 < L < -0.95$ r.l.u. and (b) $-0.55 < L < -0.45$ r.l.u., and shown with an offset of 15 for clarity. Solid lines show the fits discussed in Secs. S4 and S5.

To quantify the remaining interchain correlation effects, we fit the intensity measured at 35 K to a weighted sum of the isolated-chain response, taken from DMRG at 35 K, and the response of the thermally disordered system with a realistic average segment length of $\langle n \rangle = 10$ sites and the value $\epsilon_1 = 0.101(2)$ given in Table S1. In this fit we also include the actual energy and momentum steps of the experimental data binning, which is responsible

for the discrepancy in shape between the smooth model of Fig. S6(c) and the more discrete “disordered coupled chains” response in Fig. 4(a) of the main text.

The results of this procedure, shown by the red lines in Figs. 4(a) and 4(b) of the main text, indicate that approximately 63% of the measured response can be ascribed to residual interchain correlations, with a systematic error of order 5%. Although this seems to be a surprisingly large fraction, it should be borne in mind that essentially all of the chains are correlated below T_{N1} , which is only 7 K lower, because with a random field there is no longer any cancellation effect of the type determining the response of 2/3 of the Ising chains in the FI phase. As noted in the main text, susceptibility measurements indicate that these correlations persist up to temperatures around 80 K in RbCoCl_3 while diffuse scattering measurements [28] confirm their presence up to 60 K.

We now step back to consider the physics of the system. In Fig. S7 we illustrate the evolution of the dynamical structure factor with temperature by comparing the zone-center and zone-edge intensities at all three measurement temperatures. This highlights the rapid loss of the bound-state (staggered-field) contributions, the broadening of both the continuum and the remaining bound-state signals, and the upshift of the lower part of the band that can be understood as a narrowing effect due to the scattering of propagating domain-wall pairs on thermally excited domain walls. Figure S7 allows a clear visualization of the way in which the Matsubara (domain-wall) description allows these changes to be captured by only two thermal parameters (for line width and band width) and highlights the power of state-of-the-art DMRG methods to compute the full response of 1D systems at finite temperatures and energies.

For perspective on our modelling of the 3D Ising system, the Matsubara and DMRG methods are complementary in that DMRG provides the fundamental strongly correlated quantum physics, albeit at significant computational expense, which makes it difficult to perform iterative fits of experimental data and prohibitive to include randomness; the extended Matsubara (effective Hamiltonian) framework is cheap and easy to apply for iterative fitting, but its approximate inclusion of thermal effects requires a benchmark that DMRG can provide.